

Decreasing the Cost of Morphing in Adaptive Morphogenetic Robots

Luis A. Ramirez, Robert Baines, Bilige Yang, and Rebecca Kramer-Bottiglio*

Recent advances in locomoting robotics have demonstrated how shape morphing can enhance efficiency, mobility, and speed during transitions between domains, such as from land to water. However, prior approaches often optimize a robot's propulsor shape, stiffness, and gait to minimize the cost of transport in distinct domains while neglecting the energy required to achieve these shape and stiffness changes at domain interfaces. Additionally, many shape-morphing robots rely on thermally driven materials that couple shape and stiffness changes to environmental temperatures, limiting their applicability in real-world multidomain scenarios. This work introduces the Jamming Amphibious Robotic Turtle (JART), which employs pressure-responsive, topologically altered kirigami laminar jamming to transform its limbs between hydrodynamic flippers and load-bearing legs. Energetic analyses reveal that JART achieves a 98.5% reduction in the energetic cost of morphing compared to thermally driven predecessors. Its pressure-responsive morphing mechanism also enables temperature-independent energy expenditures when morphing, rapid stiffness switching, decoupled control of stiffness and shape, and robust postloading shape recovery. System-level evaluations highlight JART's ability to efficiently transition between domains, demonstrated through a continuous terrestrial-aquatic-terrestrial transition at an ocean inlet. This study provides valuable insights into the design of deployable, multidomain robots, advancing their potential for real-world applications.

robots, biological systems exhibit phenoplasticity in anatomical structure, stiffness, and overall behavior. Broad adaptation affords many animals the ability to navigate multiple environments and accommodate a variety of tasks.

In response to the performance gap between biological systems and robots, the field of soft robotics has sought material-based solutions to endow robots with enhanced abilities for environmental adaptation. Innovations have led to improved mobile robot performance via devolving high-level computation to passive mechanical features^[7,8] or leveraging active shape and stiffness-changing robot components.^[9,10] For example, exploiting passive body compliance has enabled robots to locomote over rocky, uneven terrain,^[11,12] transit-constrained spaces,^[13,14] operate in hazardous zones,^[15] and interact with delicate ecosystems.^[16] Toggling shape and stiffness changes in materials have empowered robots to modify their limb shapes to expand their reachable workspace,^[17] and even switch between favorable bodily forms for locomotion in multiple environments.^[18]


When traversing multiple environments, such as the aquatic-to-terrestrial transition, shape-morphing mobile systems have demonstrated the ability to specialize propulsor shapes to meet changing physical demands.^[19] For instance, leveraging shape-morphing limbs and adaptive gaits within a single robotic platform with unified structural and actuation systems—a design paradigm termed adaptive morphogenesis^[20]—has been shown to improve efficiency,^[21] speed,^[22] and mobility^[23] across aquatic and terrestrial domains. However, prior works have notably lacked quantification of morphing efficiency at domain interfaces, which is primarily governed by the energetics of the shape-morphing mechanisms.

Many current shape-changing robots utilize thermally activated actuators and variable-stiffness materials, including nylon twisted-and-coiled actuators,^[24] shape memory alloys,^[25,26] liquid crystal elastomers,^[27,28] thermoset epoxies,^[21,29] and thermoplastics.^[22,30] These systems rely on heating above a critical transition temperature to induce shape change, which introduces several limitations. For example, Joule heating can incur high energy costs or fail entirely under forced convection boundary conditions, such as in flowing water or cold air.^[21] Moreover, the thermal dependence often couples shape and stiffness changes (e.g.,

1. Introduction

Mobile robots are impacting sectors as diverse as search and rescue,^[1] environmental monitoring,^[2] and the home service industry.^[3] The majority of mobile robots are designed to operate in a single environment; consequently, their bodies comprise dedicated mechanisms and materials, such as flexible paddles or rigid wheels, and their behaviors are programmed to perform efficiently only in that specific niche.^[4–6] Unlike many mobile

L. A. Ramirez, R. Baines, B. Yang, R. Kramer-Bottiglio
School of Engineering & Applied Science
Yale University
9 Hillhouse Avenue, New Haven, CT 06511, USA
E-mail: rebecca.kramer@yale.edu

 The ORCID identification number(s) for the author(s) of this article can be found under <https://doi.org/10.1002/aisy.202401055>.

© 2025 The Author(s). Advanced Intelligent Systems published by Wiley-VCH GmbH. This is an open access article under the terms of the Creative Commons Attribution License, which permits use, distribution and reproduction in any medium, provided the original work is properly cited.

DOI: 10.1002/aisy.202401055

heating a shape memory polymer reduces its stiffness while inducing stress relaxation), which can negate the locomotor advantages of on-demand stiffness adjustments.^[31,32] Additionally, thermally activated materials are often brittle, making them susceptible to failure under the dynamic perturbations encountered in multidomain environments.^[33,34]

We introduce the Jamming Amphibious Robotic Turtle (JART; Figure 1a–d), a bio-inspired robot designed for locomotion across terrestrial and aquatic environments. Inspired by the limbs of sea turtles and land tortoises, JART's limbs transform between hydrodynamic flippers optimized for swimming and load-bearing legs designed for terrestrial mobility. This transformation is achieved using a pressure-responsive, kirigami laminar jamming system, enabling rapid, energy-efficient, and temperature-independent shape and stiffness changes. The kirigami layer jamming approach also decouples JART's limb stiffness and shape, enabling a broader library of stiffness-shape-gait propulsion strategies that significantly reduce morphing costs at the land-water interface and maintains similar transport costs in both terrestrial and aquatic environments compared to its thermally responsive predecessor. JART additionally demonstrates repeatable postloading shape recovery, reducing catastrophic failure modes and extending deployment durations. JART's morphing sequences are 98.5% more energy-efficient, an order of magnitude faster, and significantly more robust across varied subenvironments than those of the prior Amphibious Robotic Turtle (ART).^[21] The findings of this study underscore the importance of considering energetic quantities, such as cost of morphing (COM) and the multienvironment cost of transport, in the design of future shape-morphing, multidomain robots.

2. Results and Discussion

2.1. Robot Design

JART is a 0.33 m-long, 6.6 kg tethered quadruped with a turtle-like body plan consisting of a 3D-printed shell, chassis, four three-degree-of-freedom joints, as well as four morphing limbs (Figure S1a, Supporting Information). Each shoulder joint has three motors arranged in a kinematic linkage to achieve up/down, forward/backward, and angle of attack movements, defined as θ , ϕ , and α , respectively (Figure S1b, Supporting Information). JART's key feature, its morphing limbs, modulate between a streamlined flipper and a columnar leg shape through a move-and-hold actuation system. Morphing JART's limbs between flipper and leg states is achieved using fiber-reinforced pneumatic actuators and variable stiffness jamming layers, which are enclosed in a membrane and adhered to the actuators. At atmospheric pressure, the encapsulated layers slide freely and remain flexible, while applying vacuum compresses them and increases frictional coupling, thereby increasing rigidity.^[35] Once the desired limb morphology is achieved through actuator inflation or deflation, an external vacuum pump removes air from the jamming membrane, stiffening and locking the limb's shape with minimal impact on the actuation-induced curvatures.

We initially selected laminar jamming technology as the variable stiffness component in the limbs because of its temperature-independence, rapid stiffness transitions, and postload recovery capacity simply by un-jamming and re-jamming. However, with the goal of building limbs that switch between extremes of geometry and stiffness, we noted that the flexural stiffness ratio of jammed to unjammed states in conventional laminar jamming systems scales with the square of the number of layers n in the

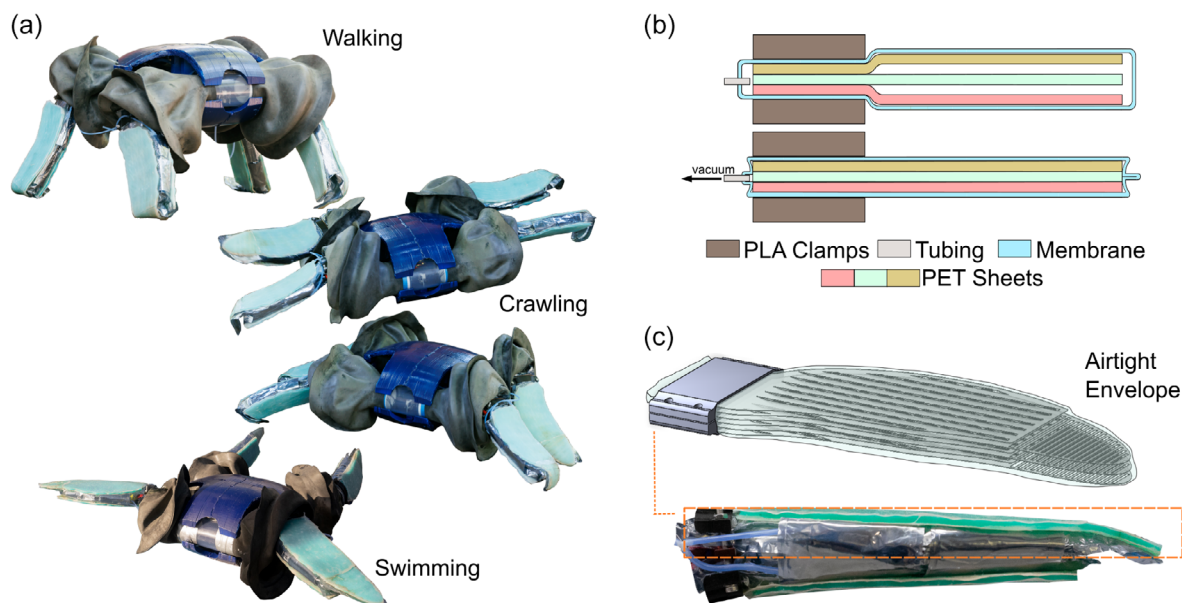


Figure 1. Shape morphing limbs with kirigami layer jamming. a) JART walking, crawling, and swimming by switching between flipper and leg configurations and changing its gaits. Scale bar: 10 cm. b) Schematic of layer jamming limb. Multiple layers are encased in an airtight envelope and clamped together at their base. Upon application of vacuum, layers agglomerate and yield high shear strength through friction, increasing the flexural stiffness of the limb. c) Computer-aided design of half of a limb, encompassing both long and short kirigami-cut layers in an airtight envelope alongside image of morphing limb in flipper configuration.

assembly^[36] (further justification for using jamming mechanisms can be found in Note S1, Supporting Information). The same analysis reveals that increasing n has a proportional effect on the bending stiffness in the unjammed state. An increased unjammed stiffness may impede move-and-hold operations if an actuator cannot supply enough force to overcome the bending resistance of the unjammed layers. Likewise, a large number of layers will exert a restoring force that can overcome the jamming force maintaining cohesion, reducing desired curvatures in the leg configuration. These considerations motivated the design of a bespoke laminar jamming system that allows a pneumatic actuator to easily deform the limb to target configurations and, when jammed, to hold the configuration with negligible relaxation. We thus employed structured removal of material from constituent layers, a technique dubbed kirigami layer jamming.^[37]

2.2. Layer Jamming Characterization

We hypothesized that removing material from the laminar jamming sheets with kirigami techniques could provide strain relief in bending of the unjammed system, allowing the limb to readily morph between desired configurations. Prior work^[37] has shown that material removal reduces the effective cross-sectional area of jamming specimens, decreasing the moment of area and thus lowering bending stiffness. Each morphing limb comprises two halves that are bonded together about their contours. We conducted three-point bending tests on half-limb specimens, in the width direction, to find designs with a reduced flexural stiffness for limb morphing (Figure S2, Supporting Information). Designs included unaltered (neat) layers as a control, sheets augmented with a truss-like pattern of cuts to create periodic, aligned vacancies of material, and a variation of the latter with a $3\times$ increased density of cuts while maintaining a constant fraction of removed material.

The average neat specimen's force–displacement response features a drop in stiffness after the initial cohesive linear regime, indicating onset of slip (Figure 2a). Two stiffness values were calculated from the force–displacement curves: an initial preslip stiffness (from the slope of the graph at 2 mm) and a secant stiffness (from the slope of a line connecting the forces at 0 and 14 mm). The initial stiffness encompasses expected deflections of the limb when equipped to the robot, while the secant stiffness illustrates the mechanical influence of the kirigami augmentations at deflections that approach failure.

Removal of material decreases both the jammed and unjammed initial stiffnesses relative to those of the neat specimen by 3.9 and 51.1%, respectively (Figure 2b,c, Supporting Information). The cut pattern with $3\times$ more cut density exhibited even larger decreases, 49.7 and 83.7% in jammed and unjammed initial stiffnesses relative to those of the neat specimen, respectively (Figure 2c, Supporting Information). Although a lower unjammed stiffness would enhance the ability to morph to target configurations, the corresponding jammed stiffness decrease reduces the maximum load capacity, which is not desirable for the morphing limb. Furthermore, a high density of material removal in concentrated areas results in specimens that slip at lower deflections because of reduced interlayer contact area.

To mitigate jammed stiffness that decreases and early-onset slip that occurs with material removal, we offset the cut patterns in every other layer such that no continuous vacancies of material arose through the thickness of the sheet stack (Figure 2d). In doing so, we sought to remove the compliant hinge-like material formed between aligned vacancies that reduce the jammed stiffness, and simultaneously increase the interlayer contact area. Repeating three-point bending tests on these specimens revealed that layers with offset cuts selectively decrease both initial and secant unjammed stiffnesses while preserving comparable jammed stiffnesses to neat sheets (Figure 2e,f). The effect is exacerbated for higher cut densities. Implementing offset cuts, the initial flexural stiffness differential between jammed and unjammed states of the limb was successfully amplified by $4\times$ relative to neat layers (Figure 2g). The secant stiffness jamming ratios of offset specimens were likewise amplified up to $4\times$ that of the neat specimen (Figure 2h). Table 1 and S1 (Supporting Information) tabulate all of the initial and secant jamming ratios.

Overall, offset cuts with a high density of vacant material optimize specimens' jamming ratios by decreasing the unjammed stiffness and negligibly impacting the jammed stiffness (impacts of kirigami augmentations are further discussed in Note S2, Supporting Information). The decreased unjammed stiffness allows the adhered pneumatic actuators to manipulate the kirigami layers into target curvatures with lower pressurization, and then apply jammed stiffness akin to unaltered layers. The result is a reduced shape-morphing energy, linked to the reduced unjammed bending stiffness of the collated kirigami layers which can be effectively morphed with lower energy actuators (Movie S1, Supporting Information).

2.3. Limb Evaluation

Having identified a kirigami layer jamming design that enhances the flexural stiffness differential of jammed to unjammed states relative to that of neat layers, we proceeded to create a full limb prototype to evaluate its capacity to withstand compressive loads. We conducted compression loading cycles on the jammed leg configuration at angles that it would encounter during terrestrial locomotion when equipped to the robot (Figure 3a,b). The leg was compressed until it buckled or the force readout from the loadhead began to decrease, indicating deviation from the original load-bearing cross-section. Between compression cycles, limbs were unjammed, manually remorphed into their leg configuration, and then jammed into the leg configuration again.

The leg's maximum average sustained loads at 0, 15, and 30° were 380, 95, and 65 N, respectively (Figure 3c). The decrease in maximum sustained load with increasing angle corresponds to the increasing radial component of force imparted by the loadhead that flattens the limb halves. Over the ten cycles, the maximum sustained load exhibited, at the most, a spread of 150 N. Up to the first 40 mm of deflection, this spread is a highly repeatable 20 N (Figure 3c; Figure S3, Supporting Information). Juxtaposing the leg and flipper configurations' compression responses highlights the ability of kirigami layer designs to hold a geometrically stiffer circular cross-section; in fact, the leg withstood 150 N more force than the flipper (Figure S4, Supporting Information).

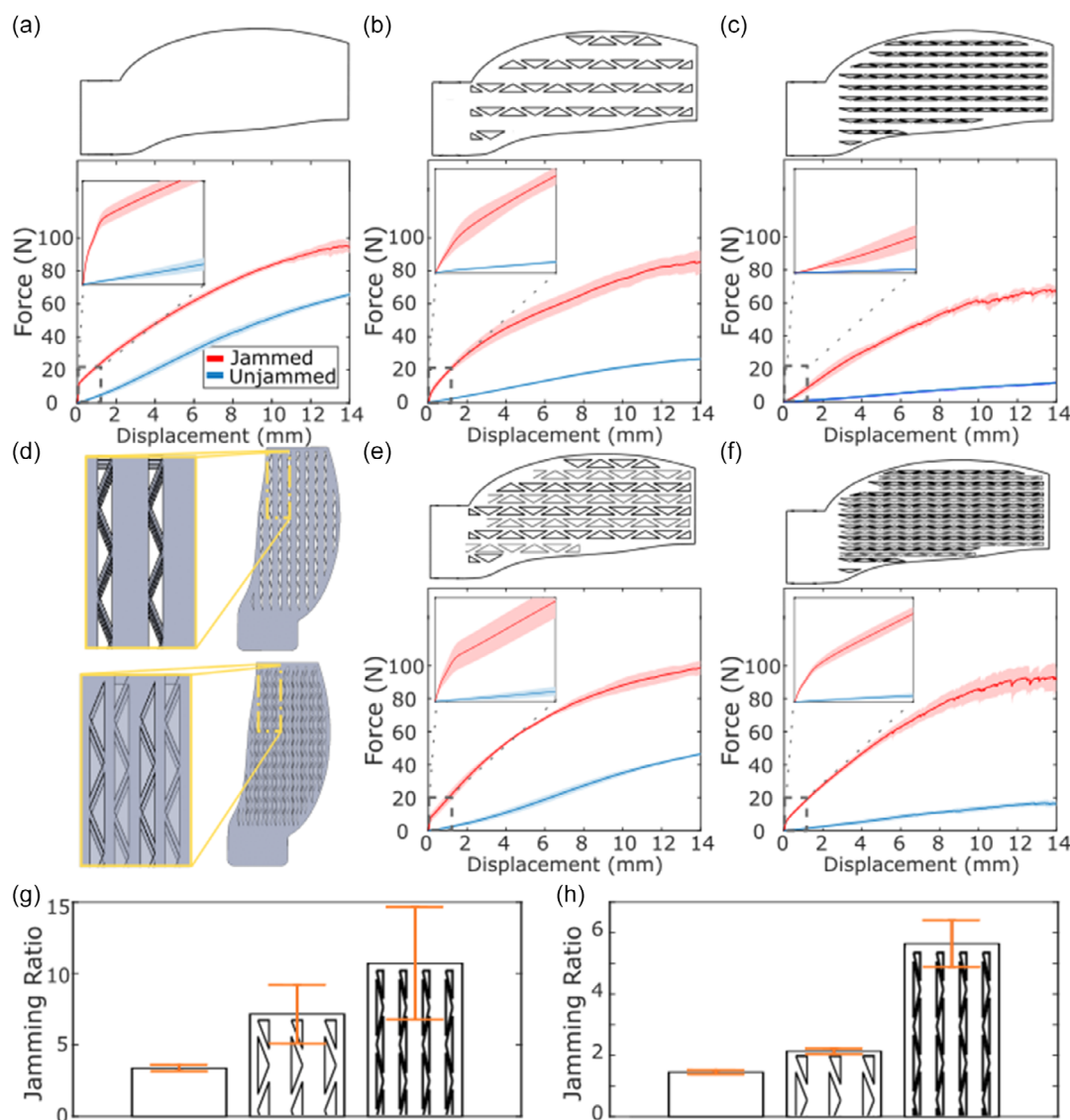


Figure 2. Characterization of kirigami layer jamming sheets. a) Three-point bending of neat (unaltered) flipper into cylindrical curvature. Inset gives a zoomed-in view of the preslip regime. Error clouds represent ± 1 SD of 6 trials. b,c) Three-point bending of aligned kirigami with increasing cut density. The removal of material results in a proportional decrease in unjammed stiffness and jammed preslip stiffness. Insets give zoomed-in views of the preslip regime. Error clouds represent ± 1 SD of 6 trials. d) Illustrations of aligned and offset jamming layer designs with the highest cut density. e,f) Three-point bending of offset kirigami designs, with increasing cut density, demonstrating an increase in jammed preslip stiffness and decrease in unjammed stiffness. Insets highlight the preslip regime. Error clouds represent ± 1 SD of 6 trials. g) Initial jammed to unjammed flexural stiffness ratios for the neat control and offset designs of varying cut density. Initial values collected from ≈ 2 mm. Error bars represent the average of 6 trials with ± 1 SD deviation from the mean. h) Secant jammed to unjammed flexural stiffness ratios for the neat (control) and offset designs of varying cut densities. Values collected from ≈ 14 mm. Error bars represent the average of 6 trials with ± 1 SD deviation from the mean.

Further insight into the behavior of the leg under compression can be gleaned by inspecting regimes in its force–displacement curves at the various tested angles. The limb’s short wall, long wall, and curled foot subcomponents each play different roles during compression (Figure 3b). Across all angles, the curled foot readily deforms upon contacting the loadhead, exhibiting low stiffness. It deforms until it impacts the short wall, upon which a steep increase in force is observed. In contrast, the influence of the short and long walls of the limbs is sensitive to

loading angle, causing distinct variations in stiffness, maximum sustained force, failure modes, and slipping of the layers at higher displacements (Figure 3d–f). For instance, at a zero-degree (purely axial) loading angle, both the short and long walls contact the loadhead at the same time. They are then pushed radially outward, eventually buckling at a critical loading force (Figure 3d). At a loading angle of 15° , the short wall layers slip and begin to buckle before those of the long wall, manifesting as a temporary dip in force. Further displacement sees an increase

Table 1. Initial jamming ratios, jamming stiffnesses, and unjammed stiffnesses of laminar jamming specimens with neat (unaltered), kirigami cut, and kirigami with 3× cut density designs.

Kirigami design	Jammed stiffness [N mm ⁻¹]	Unjammed stiffness [N mm ⁻¹]	Jamming ratio
Neat	15.1	4.2	3.4
Aligned kirigami	14.5	2.1	6.9
Offset kirigami	16.1	2.2	7.1
Aligned kirigami 3×	7.6	0.7	10.2
Offset kirigami 3×	13.7	1.3	10.7

in force as the flattened short wall impacts the long wall (Figure 3e). At an even greater loading angle of 30°, the failure mode is less abrupt. Both walls gradually flatten as a function of increasing displacement (slip initiation in each wall is highlighted with circular black markers in Figure 3f).

Compression test results confirm that a single limb can sustain the entire 64 N weight of the robot at all the loading angles. Although the mechanics of deformation vary based on the angle of environmental contact, the small spread in data over the ten cycles illustrates that consistent loading performance can be maintained through repeated cycles of limb buckling and recovery. Requisite to such promising compression performance of the limb is a hermetically sealed membrane around the layers to retain the pressure differential enforcing a jammed state. Measuring the relaxation of a limb cross-section's diameter after terrestrial-to-aquatic transition field tests with the robot, we found that diameter decreases by only 5% over a nine-hour period (Figure S5, Supporting Information). Thus, JART's morphing limb not only reliably supports more than the weight of

the robot and exhibits postload recovery capacity, but also robustly holds its stiffness and shape.

2.4. Morphing Energetics and Speed

Beyond mechanical robustness, multidomain robotic systems must achieve net efficiency gains from their morphing operations to perform effectively across diverse settings. In other words, a robot's energetic COM should be less than the excess energy it would expend during locomotion if the robot did not morph. We split JART's COM into subterms to see the relative contributions of different sources of energetic cost:

$$COM = E_{\alpha} + E_{\beta} + E_{\gamma} \quad (1)$$

where E_{α} is the energy consumed by the actuators performing shape change, and E_{β} , E_{γ} are specific to robots implementing variable stiffness materials and mechanisms to change shape: E_{β} is the energy consumed by softening, and E_{γ} is the energy consumed by stiffening. Note that this expression assumes COM has units of energy, although it could be normalized by mgv to become dimensionless (for direct comparison to dimensionless cost of transport values). An explanation of the COM terms for JART and other shape-morphing robots can be found in Figure S6 and Note S3 (Supporting Information).

We calculated the COM terms for JART as well as its predecessor, ART (Figure 4a). Both robots use identical pneumatic actuators driven by a compressor that consumes $E_{\alpha} = 70$ J to actuate all limbs. ART requires an E_{β} of 10 290 J—99.3% greater than JART's E_{γ} (Figure 4b). Furthermore, constant energy must be input to keep ART's limbs soft, and when submerged in 25 °C water, ART's E_{β} is 46.25% higher due to free convection (Figure 4b). ART passively cools its limbs to re-stiffen, resulting

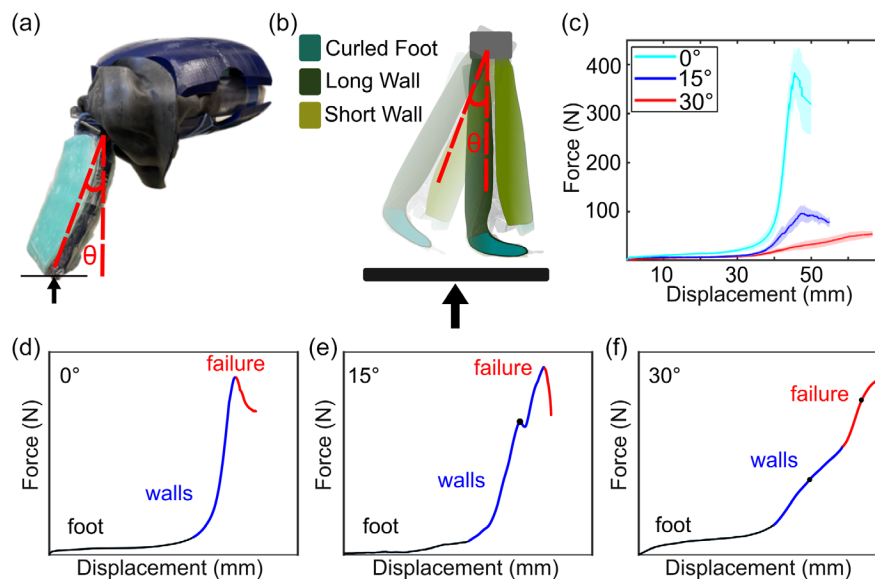


Figure 3. Morphing limb leg configuration characterization. a) Leg loading experienced during walking gaits. b) Schematic of the compression test setup as well as various subcomponents of the morphing limb. c) Axial compression tests at various angles to measure the maximum loading capabilities of limbs before failure. Solid lines indicate an average of ten trials. Error clouds represent ± 1 SD from the mean. d–f) Different limb compression regimes at 0, 15, and 30°, respectively.

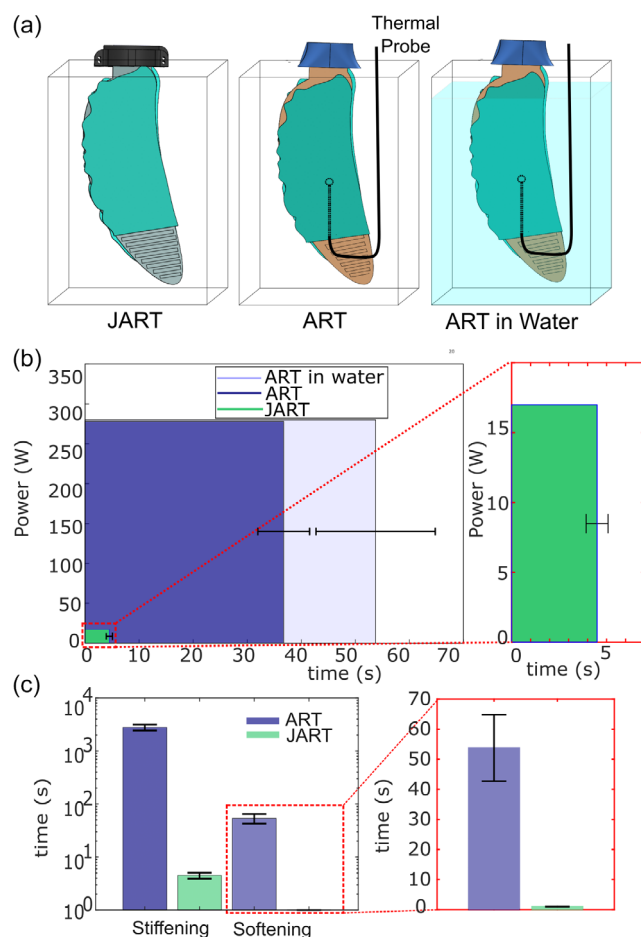


Figure 4. COM analysis. a) Schematic representing the test setup to measure the COM. A thermal probe is placed between the two thermoset walls to measure when glass transition temperature is reached. b) Energy input is measured during stiffness modulation of the limbs for JART, ART in air, and ART in water. c) Graph comparing the time required by the variable stiffness systems to undergo stiffening and softening. Values were calculated from four trials with error bars representing 1SD from the average.

in $E_\gamma = 0$. In contrast, JART's limbs passively equilibrate to atmospheric pressure, meaning that its $E_\beta = 0$. Once JART's limbs are actuated into their leg shape, an E_γ of 76.5 J is required to lock the shape into place. JART's morphing performance is furthermore unaffected by being submerged underwater or exposed to cold temperatures.

More insight into morphing energetics can be gained by analyzing the three distinct shape change sequences that JART and ART undergo: 1) flipper-to-leg, ($COM = E_\alpha + E_\beta + E_\gamma$); 2) leg-to-rigid-flipper, ($COM = E_\beta + E_\gamma$); and 3) leg-to-compliant-flipper, ($COM = E_\beta$). In the flipper-to-leg sequence, ART and JART reach their largest COM values of 10 360 and 146.5 J, respectively. In the leg-to-rigid-flipper sequence, these values stand at 10 290 and 76.5 J. Finally, for the leg-to-compliant-flipper sequence, ART requires continuous energy consumption to retain a compliant state, resulting in its COM approaching ∞ . In contrast, JART's limbs' default compliant state implies that its leg-to-compliant-flipper COM is zero.

These energetic measurements not only highlight the energetic improvement of JART's compared to ART, but also introduce unique shape change sequences that require no energy input to adapt to multidomain transitions, i.e., JART's leg-to-compliant-flipper sequence.

Another pertinent consideration for shape-morphing robots is the time it takes them to switch between functional configurations. While ART took ≈ 2800 s, JART can stiffen its limbs in 4.5 s (Figure 4c). While relaxing the limbs took an elevated 50 s for ART, JART relaxes its limbs within 1 s when vacuum is released. The adoption of laminar jamming increases the stiffening and softening speeds of JART's limbs by $\approx 621\times$ and $53\times$, respectively, compared to ART's thermally responsive limbs. This stiffness change achieved within seconds allows for rapid adaptations to environmental transitions in the wild.

2.5. System Locomotion Performance

To verify that the limb's favorable load-bearing and morphing capabilities do not come at the expense of system-level performance, we evaluated JART's cost of transport (COT) when walking, swimming, and crawling:

$$COT = P_{in}/mgv \quad (2)$$

where P_{in} is the electrical power consumption of the motors during the gaits, m is the mass of the robot (excluding off-board, tethered components), g is the gravitational acceleration constant, and v is the robot's forward velocity as discerned from high-definition video footage. Additionally, we studied the impact of decoupled shape and stiffness on COT for the swimming and crawling gaits, with limb stiffness constrained to binary jammed or unjammed states.

2.5.1. Walking

JART walks with its limbs morphed into their leg configuration and using a statically stable creep gait in which three of its limbs contact the ground at any moment (Movie S2, Supporting Information). While walking, the front left and right shoulders draw the majority of current (Figure S7a, Supporting Information). Plateaus in current occurs for the swing forward (ϕ) motor, corresponding to motor stall. Although the forward-leaning posture JART assumes during the gait concentrates most of its weight on the front two limbs, periodically causing stall, we found that such a posture was the most stable and facilitated the highest speeds: JART's average walking COT is 15.4 and it maintains an average speed of 0.03 m s^{-1} (0.09 bl s^{-1}). The leg configuration provides sufficient load-bearing capacity, and the curled foot passively deforms to the substrate, allowing JART to walk on unstructured substrates without the need for closed-loop gait control.

2.5.2. Swimming

JART swims with its limbs in the flipper configuration, using a turtle-inspired paddling gait. The fore-flippers engage in movement, while the rear flippers remain stationary, mimicking the swimming behavior observed in turtles in the wild (Figure S7b;

Movie S3, Supporting Information). We recorded COT data with the flippers in both jammed and unjammed states. To isolate the effect of limb stiffness on COT, we conducted all experiments using a consistent gait at a fixed speed. The current drawn during swimming in both states was equivalent, as was the robot's average velocity, at 0.12 m s^{-1} (0.36 bl s^{-1}). Consequently, jammed and unjammed swimming states both had an average COT of 1.60. Although we did not vary swimming speed in this study, prior work suggests that softer fins improve efficiency at lower speeds.^[38]

We utilized a flow tank to measure the hydrodynamic forces on the flipper at various flow rates and angles of attack (Figure S8, Supporting Information). We conducted experiments at flow rates of 0.3 and 0.4 m s^{-1} , which coincide with JART's flipper velocities when swimming. Drag monotonically increased as a function of the angle of attack, α . There was no substantial difference between drag forces when jammed or unjammed. Lift, in contrast, was not monotonic in either stiffness state. When jammed, the flipper produced multiple distinct peaks of lift, centered around $\alpha = 5, 15$, and 40° . As one example, at 40° and 0.3 m s^{-1} , the jammed state exhibited $4.7\times$ more lift force than the unjammed state. The peaks in lift in the jammed state can be attributed to the stiffer flipper's ability to, at certain angles, sustain the flow-induced pressure differential between top and bottom surfaces without deforming.^[39] The unjammed flipper occasionally exceeds the lift of the jammed flipper, such as the case of $\alpha = 30^\circ$ at 0.3 m s^{-1} . Fluctuations in lift generation based on the stiffness state suggest that active stiffness control, in tandem with switching between drag-based and lift-based swimming regimes, could facilitate optimal swimming efficiency.

2.5.3. Crawling

JART's transitional crawling gait was evaluated for both jammed and unjammed flipper states over lab floors, grass, sand, and

rocks (Figure 5a). On our lab floor (porcelain tiles), JART's unjammed COT value was nearly $2\times$ greater than the jammed one. The disparity between jammed and unjammed performances diminishes as the substrate becomes increasingly unstructured and, in fact, on rocks, the unjammed state boasts a $1.35\times$ lower COT than the jammed state. We noticed that the unjammed limbs conform to unstructured terrains, expanding their interfacial contact area. In contrast, jammed limbs rigidly interact with the environment, as a single edge concentrates the force exerted by the robot's body weight. On loose or granular substrates, this can lead to substrate fracture, reducing the effectiveness of forward propulsion.^[40,41] Substrate fracture is particularly noticeable as the robot propels itself over rocks and sand (Movie S4, Supporting Information). Experimental results from JART indicate that switching between different stiffness states can enhance transport efficiency across certain, and potentially unstructured, terrains.

2.5.4. Transitions in the Field

Boasting efficient locomotion on land, in water, and across transitional zones, JART combines functional shapes, stiffness states, and gaits to transition between terrestrial and aquatic environments (Figure 5b). As shown in Movie S5 (Supporting Information), JART successfully walks on packed dirt along the bank of an estuary—a capability beyond that of its predecessor, ART. Approaching a muddy region at the water's edge, where stable traversal with a walking gait becomes challenging, JART switches to a crawling gait with its limbs in a jammed state. This configuration mitigates slipping by minimizing substrate interactions that would occur with compliant flippers. Once sufficiently submerged, JART transitions its limbs into a jammed flipper state to generate power strokes, propelling itself into the river's center. When its trajectory is unexpectedly obstructed by submerged rocks, JART adapts by unjamming

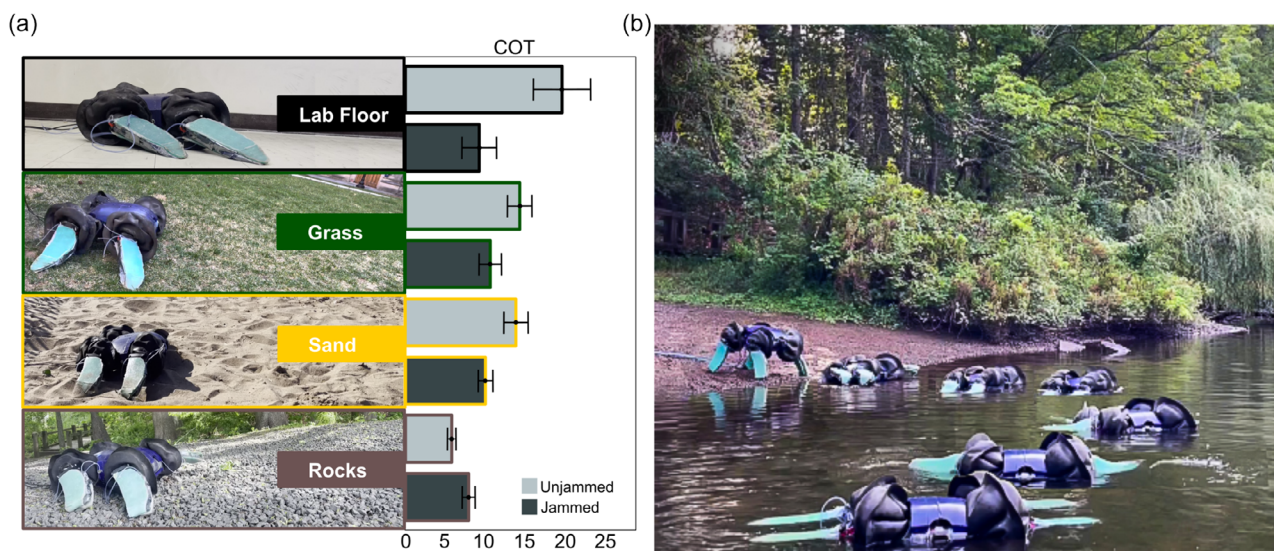


Figure 5. Crawling performance through transitional zones. a) Images of JART crawling on substrates, juxtaposed with the COT performances in jammed and unjammed leg and flipper states. COT values were calculated from at least five trials. Error bars represent $\pm 1\text{SD}$ from averaged values. b) Composite image with superimposed snapshots of JART walking, crawling, and swimming in an estuary.

its limbs into a compliant flipper state. This flexibility enables it to deflect off the rocks while using a crawling gait to regain momentum. Freed from the obstruction, JART turns landward, swimming toward a transition zone covered with pebbles. Upon reaching this area, JART employs its unjammed flippers and a crawling gait to distribute its weight evenly, preventing substrate fracture as it crawls out of the water. JART's rapid, temperature-independent, and robust shape changes—enabled by decoupled shape and stiffness in its flipper states—allow it to readily adapt to the physical challenges of terrestrial-to-aquatic transitions, enabling smooth movement between land and water.

3. Conclusion

We introduced JART, a next-generation amphibious robot with shape-morphing, variable-stiffness limbs, designed to achieve efficient multidomain locomotion. Through laboratory studies and field deployments in an estuarine environment, we gained key insights into improving energy efficiency and adaptability for robots traversing land and water combinatorial environments.

To address the limitations of temperature-dependent morphing in JART's predecessor, ART, we leveraged laminar jamming technology. Traditional laminar jamming designs proved inadequate for achieving the desired geometric transformations, prompting us to enhance the limb design with offset kirigami cuts in the constituent layers. This approach effectively reduced the component's unjammed stiffness without compromising jammed stiffness, enabling JART to morph its limbs between flipper and leg states.

JART's jamming limbs demonstrated resilience to failure, as they buckle under extreme loads instead of fracturing or undergoing plastic deformation. This failure mode, caused by interlayer slipping, is fully reversible; releasing vacuum and reapplying it restores the limb to its original state. Unlike thermally driven systems, the stiffening and softening of JART's limbs depend solely on the volumetric flow rate of air, allowing for rapid and consistent transitions. JART achieves stiffening and softening speeds $\approx 621\times$ and $53\times$ faster, respectively, than ART. Additionally, the energy required to induce stiffness changes is reduced by 99.3%, resulting in a 98.5% decrease in the COM for limb transitions. In some cases, such as switching between stiff and compliant flippers, the COM is effectively zero, allowing energy-free, on-demand adaptability to environmental changes.

JART's ability to toggle flipper stiffness and adjust gaits significantly enhances its performance in challenging environments. For example, on packed rocks, switching to an unjammed flipper state and adopting a crawling gait reduced the COT by mitigating substrate yielding. These findings align with previous studies that highlight the energetic advantages of integrating jamming systems into legged robots, where stiffness modulation improves traction, dampens vibrations, and optimizes limb-environment interactions.^[42–44] Hydrodynamic tests further suggest that flipper stiffness can serve as a dynamic control input, reducing swimming COT by stiffening during power strokes and slackening during recovery strokes.

By demonstrating energy-efficient, temperature-independent shape morphing, JART exemplifies how innovations in decoupling limb shape and stiffness, coupled with significant

reductions in morphing cost, can elevate the performance of multidomain robotic locomotion. These advances mark a critical step toward robust, adaptive, and energy-efficient robots capable of navigating complex terrestrial, aquatic, and transitional environments.

JART's performance metrics reported herein were achieved using off-board air compressors and vacuum pumps, as the robot remained tethered throughout this study. Future work will focus on untethering JART^[45] (see Note S5, Supporting Information), incorporating environmental sensing for autonomous decision-making, and implementing closed-loop stiffness control for continuous modulation beyond the current binary states. Additional efforts will aim to design hardware capable of withstanding extreme conditions such as high-energy waves, flowing granular media, and impacts with rocks—challenges inherent to multidomain transitions (see Note S5, Supporting Information). Further discussion on laminar jamming technology, cost of morphing, and system breakdown can be in the Supplementary Information.^[46–55]

4. Experimental Section

Limb Construction: The robot and limb construction processes are illustrated in Figure S9 (Supporting Information). The morphing limbs are composed of three main components: polyethylene terephthalate (PET) layers, heat-sealed antistatic bags (McMasterCarr, 4663T9), and silicone pneumatic actuators (fabricated with Dragon Skin 10A, Smooth-On). Layers of the jamming assembly were laser cut from 0.01 in heat-pressed PET layers. A full limb is made from a short and long airtight envelope that encases augmented PET layers. The shorter envelope contains thirty short layers, whereas the longer envelope holds twenty-five short layers and five long layers. The long layers have a different kirigami pattern at their tip that facilitates curling. Detailed manufacturing processes are presented in Note S6 and S7 (Supporting Information).

Mechanical Testing: An Instron 3345 material tester with a 1 kN load cell with a displacement rate of 40 mm min^{-1} was utilized for characterization of layers and full limbs. To measure the force required to bend layers length-wise into a cylindrical shell, we conducted three-point bending tests on specimens with 20 layers. We set the total displacement to 14 cm with a span of 6 cm. We conducted five trials for each specimen. For limb compression tests, we utilized a custom-built mounting unit to vary the loading angle. Compression tests were conducted to until substantial buckling or relaxation of the limbs occurred. Upon failure, vacuum was released and limbs were manually remorphed into the leg configuration. We conducted 10 total trials on a limb specimen for each angle. Three-point bending tests were performed width-wise on the jamming specimens to measure the force needed to induce a desired curvature and estimate the forces at which said curvature would be compromised. Once desired curvature is lost, the load-bearing abilities of a limb are markedly reduced. Continuous vacuum was supplied for all three-point bending and compression tests to ensure a pressure at $\approx 80\text{ kPa}$. All mechanical testing setups are depicted in Figure S10 (Supporting Information).

Locomotion Characterization: Walking COT experiments were carried out on a lab floor made of porcelain. Swimming COT experiments were conducted in an outdoor pool of $9 \times 4.5\text{ m}$ area and a depth of 1 m. Crawling experiments included substrates found in aquatic-to-terrestrial transitional zones, such as grass, sand, and compact rocks. Testing on sand and rocks took place at a beach and river inlet, respectively. Similar gaits to those used in ART were selected to ensure a direct comparison of locomotion performance, allowing us to evaluate whether the laminar jamming morphing limbs in JART result in improved or diminished performance.

Continuous vacuum was provided to limbs throughout walking and jammed-state crawling gaits to ensure that a completely stiff state was

maintained during data collection. We allowed the robot to reach a steady velocity before collecting data for each trial with a high-definition camera. Velocity was calculated by measuring the distance between the robot's center of mass points after an allotted period of time.

Morphing Energetic: Morphing energetics were collected in two different ways for the prior ART and current JART robots. For ART, a digital thermocouple temperature thermometer (Proster) was placed inside the limbs to record the temperature of the thermoset polymer. For JART, a stiffened state was induced with the use of a 30 L min⁻¹ vacuum pump (LAB FISH). ART's softened state was achieved by Joule-heating with a DC power supply (Korad KA3005P). The power consumed by each of these devices was measured with a plug-in power recorder (Zhurui PR10). The time used to calculate ART's morphing energy was collected as the duration of the transition from 25 to 45 °C. The softening time is recorded as the time needed for a limb to cool down from 45 °C to around 28 °C. JART's morphing energy was calculated as time needed for each limb to reach full vacuum. The submerged limb testing was performed at 25 °C water. Data collected for JART consisted of one trial for four different limb specimens whereas all four trials of ART were done on its most efficient limb. All other limbs were unable to reach the glass transition temperature when submerged under 25 °C water.

Supporting Information

Supporting Information is available from the Wiley Online Library or from the author.

Acknowledgements

This project was sponsored by the Office of Naval Research under (awards N00014-21-1-2417 and N00014-24-1-2162). Any opinions, findings, and conclusions or recommendations expressed in this material are those of the authors and do not necessarily reflect the views of the Office of Naval Research. LAR was supported by an NSF Graduate Research Fellowship (DGE-1752134). RB is now with the Department of Mechanical and Process Engineering, ETH Zurich, and additionally acknowledges The Branco Weiss Fellowship - Society in Science, administered by ETH Zürich.

Conflict of Interest

The authors declare no conflict of interest.

Author Contributions

Luis A. Ramirez: data curation (lead); formal analysis (lead); investigation (lead); methodology (lead); project administration (lead); writing—original draft (lead); writing—review & editing (lead). **Robert Baines:** conceptualization (supporting); data curation (supporting); investigation (supporting); methodology (supporting); project administration (supporting); writing—original draft (supporting). **Bilige Yang:** conceptualization (supporting); data curation (supporting); investigation (supporting). **Rebecca Kramer-Bottiglio:** funding acquisition (supporting); methodology (supporting); project administration (supporting); resources (supporting); supervision (supporting); validation (supporting); writing—review & editing (supporting).

Data Availability Statement

The data that support the findings of this study are available from the corresponding author upon reasonable request.

Keywords

amphibious robotics, efficient robot locomotion, laminar jamming, multienvironment transitions

Received: December 3, 2024

Revised: March 14, 2025

Published online:

- [1] S. P. Yeong, L. M. King, S. S. Dol, *Int. J. Marine Environ. Sci.* **2015**, 9, 2.
- [2] E. Aucone, S. Kirchgeorg, A. Valentini, L. Pellissier, K. Deiner, S. Mintchev, *Sci. Robot.* **2023**, 8, eadd5762.
- [3] J. Forlizzi, C. DiSalvo, in *ACM SIGCHI/SIGART Conf. on Human–Robot Interaction*, Salt Lake City, UT, USA, March **2006**, pp. 258–265.
- [4] M. Raibert, K. Blankespoor, G. Nelson, R. Playter, *IFAC Proc. Vol.* **2008**, 41, 10822.
- [5] R. D. Christ, R. L. Wernli Sr, *The ROV Manual: A User Guide for Remotely Operated Vehicles*, Butterworth-Heinemann, Oxford, UK **2013**.
- [6] D. Shah, B. Yang, S. Kriegman, M. Levin, J. Bongard, R. Kramer-Bottiglio, *Adv. Mater.* **2021**, 33, 2002882.
- [7] C. Laschi, B. Mazzolai, M. Cianchetti, *Sci. Robot.* **2016**, 1, eaah3690.
- [8] Y. Tang, Y. Chi, J. Sun, T.-H. Huang, O. H. Maghsoudi, A. Spence, J. Zhao, H. Su, J. Yin, *Sci. Adv.* **2020**, 6, eaaz6912.
- [9] S. Kriegman, S. Walker, D. Shah, M. Levin, R. Kramer-Bottiglio, J. Bongard, in *Robotics: Science and Systems XV*, **2019**, ArXiv: 1905.09264 [cs], <http://arxiv.org/abs/1905.09264>.
- [10] B. H. Do, V. Banashek, A. M. Okamura, in *2020 IEEE Inter. Conf. on Robotics and Automation (ICRA)*, IEEE, Paris, France **2020**, pp. 9050–9056, ISBN 978-1-72817-395-5, <https://ieeexplore.ieee.org/document/9197237/>.
- [11] D. Rus, M. T. Tolley, *Nature* **2015**, 521, 467.
- [12] D. S. Shah, J. W. Booth, R. L. Baines, K. Wang, M. Vespignani, K. Bekris, R. Kramer-Bottiglio, *Soft Robot.* **2022**, 9, 639.
- [13] E. W. Hawkes, L. H. Blumenschein, J. D. Greer, A. M. Okamura, *Sci. Robot.* **2017**, 2, eaan3028.
- [14] P. E. Schiebel, M. C. Maisonneuve, K. Diaz, J. M. Rieser, D. I. Goldman, in *Biomimetic and Biohybrid Systems: 9th International Conf., Living Machines 2020*, Springer, Freiburg, Germany, July **2020**, pp. 300–311.
- [15] M. T. Tolley, R. F. Shepherd, B. Mosadegh, K. C. Galloway, M. Wehner, M. Karpelson, R. J. Wood, G. M. Whitesides, *Soft Robot.* **2014**, 1, 213.
- [16] B. T. Phillips, K. P. Becker, S. Kurumaya, K. C. Galloway, G. Whittredge, D. M. Vogt, C. B. Teeple, M. H. Rosen, V. A. Pieribone, D. F. Gruber, R. J. Wood, *Sci. Rep.* **2018**, 8, 14779.
- [17] H. Nakai, Y. Kuniyoshi, M. Inaba, H. Inoue, in *IEEE/RSJ Inter. Conf. on Intelligent Robots and System*, Vol. 2. IEEE, Lausanne, Switzerland **2002**, pp. 2025–2030, ISBN 978-0-7803-7398-3, <http://ieeexplore.ieee.org/document/1044053/>.
- [18] D. S. Shah, J. P. Powers, L. G. Tilton, S. Kriegman, J. Bongard, R. Kramer-Bottiglio, *Nat. Mach. Intell.* **2020**, 3, 51.
- [19] R. Baines, F. Fish, R. Kramer-Bottiglio, in *Bioinspired Sensing, Actuation, and Control in Underwater Soft Robotic Systems* (Eds: D. A. Paley, N. M. Wereley), Springer International Publishing, Cham **2021**, pp. 41–69, ISBN 978-3-030-50475-5 978-3-030-50476-2, http://link.springer.com/10.1007/978-3-030-50476-2_3.
- [20] R. Baines, F. Fish, J. Bongard, R. Kramer-Bottiglio, *Nat. Rev. Mater.* **2024**, 9, 822.
- [21] R. Baines, S. K. Patiballa, J. Booth, L. Ramirez, T. Sipple, A. Garcia, F. Fish, R. Kramer-Bottiglio, *Nature* **2022**, 610, 283.
- [22] J. Sun, E. Lerner, B. Tighe, C. Middlemist, J. Zhao, *Nat. Commun.* **2023**, 14, 6023.

- [23] T. Kim, S. Lee, S. Chang, S. Hwang, Y.-L. Park, *Adv. Intell. Syst.* **2023**, 5, 2300172.
- [24] J. Sun, B. Tighe, Y. Liu, J. Zhao, *Soft Robot.* **2021**, 8, 213.
- [25] Z. Ren, M. Zarepoor, X. Huang, A. P. Sabelhaus, C. Majidi, *Front. Robot. AI* **2021**, 8, 599650.
- [26] M. Shibata, F. Saijyo, S. Hirai, in *2009 IEEE Inter. Conf. on Robotics and Automation*, IEEE, Kobe **2009**, pp. 4375–4380, ISBN 978-1-4244-2788-8, <http://ieeexplore.ieee.org/document/5152752/>.
- [27] C. Yuan, D. J. Roach, C. K. Dunn, Q. Mu, X. Kuang, C. M. Yakacki, T. J. Wang, K. Yu, H. J. Qi, *Soft Matter* **2017**, 13, 5558.
- [28] A. Kotikian, C. McMahan, E. C. Davidson, J. M. Muhammad, R. D. Weeks, C. Daraio, J. A. Lewis, *Sci. Robot.* **2019**, 4, eaax7044.
- [29] R. Baines, S. Freeman, F. Fish, R. Kramer-Bottiglio, *Bioinspir. Biomim.* **2020**, 15, 025002.
- [30] J. Sun, J. Zhao, *IEEE Robot. Autom. Lett.* **2019**, 4, 724.
- [31] D. K. Patel, X. Huang, Y. Luo, M. Mungekar, M. K. Jawed, L. Yao, C. Majidi, *Adv. Mater. Technol.* **2023**, 8, 2201259.
- [32] W. P. Weston-Dawkes, M. T. Tolley, in *Volume 7: 46th Mechanisms and Robotics Conf. (MR)*, American Society of Mechanical Engineers, St. Louis, Missouri, USA **2022**, V007T07A045, ISBN 978-0-7918-8628-1, <https://asmedigitalcollection.asme.org/IDETC-CIE/proceedings/IDETC-CIE2022/86281/V007T07A045/1150621>.
- [33] F. Xie, L. Huang, J. Leng, Y. Liu, *J. Intell. Mater. Syst. Struct.* **2016**, 27, 2433.
- [34] I. K. Kuder, A. F. Arrieta, W. E. Raither, P. Ermanni, *Prog. Aerosp. Sci.* **2013**, 63, 33.
- [35] B. Aktaş, Y. S. Narang, N. Vasios, K. Bertoldi, R. D. Howe, *Adv. Funct. Mater.* **2021**, 31, 2007554.
- [36] Y. S. Narang, J. J. Vlassak, R. D. Howe, *Adv. Funct. Mater.* **2018**, 28, 1707136.
- [37] R. Baines, B. Yang, L. A. Ramirez, R. Kramer-Bottiglio, *Extreme Mech. Lett.* **2023**, 64, 102084.
- [38] M. Ishida, A. Abdulali, N. K. Hosseini, F. Iida, in *2024 IEEE 7th Inter. Conf. on Soft Robotics (RoboSoft)*, IEEE, San Diego, CA, USA **2024**, pp. 946–951, ISBN 9798350381818, <https://ieeexplore.ieee.org/document/10522008/>.
- [39] G. Thwapiah, L. F. Campanile, *Smart Mater. Struct.* **2010**, 19, 035020.
- [40] N. Mazouchova, P. B. Umbanhowar, D. I. Goldman, *Bioinspir. Biomim.* **2013**, 8, 026007.
- [41] J. Aguilar, T. Zhang, F. Qian, M. Kingsbury, B. McInroe, N. Mazouchova, C. Li, R. Maladen, C. Gong, M. Travers, R. L. Hatton, H. Choset, P. B. Umbanhowar, D. I. Goldman, *Rep. Prog. Phys.* **2016**, 79, 110001.
- [42] S. Hauser, P. Eckert, A. Tuleu, A. Ijspeert, in *2016 6th IEEE Inter. Conf. on Biomedical Robotics and Biomechatronics (BioRob)*, IEEE, Singapore, Singapore **2016**, pp. 1160–1165, ISBN 978-1-5090-3287-7, <http://ieeexplore.ieee.org/document/7523788/>.
- [43] S. Chopra, M. T. Tolley, N. Gravish, *IEEE Robot. Autom. Lett.* **2020**, 5, 3975.
- [44] J. Pinski, J. Brett, L. Hanson, K. L. Surdo, D. Howard, in *2022 IEEE/RSJ Inter. Conf. on Intelligent Robots and Systems (IROS)*, IEEE, Kyoto, Japan **2022**, pp. 8507–8514, ISBN 978-1-66547-927-1, <https://ieeexplore.ieee.org/document/9982171/>.
- [45] J. Sun, B. Lin, L. A. Ramirez, E. Figueroa, R. Baines, B. Yang, E. Marroquin, R. Kramer-Bottiglio, in *2024 IEEE 7th Inter. Conf. on Soft Robotics (RoboSoft)*, IEEE, San Diego, CA, USA **2024**, pp. 374–379, ISBN 9798350381818, <https://ieeexplore.ieee.org/document/10521924/>.
- [46] E. Sihite, A. Kalantari, R. Nemovi, A. Ramezani, M. Gharib, *Nat. Commun.* **2023**, 14, 3323.
- [47] S. Eristoff, S. Y. Kim, L. Sanchez-Botero, T. Buckner, O. D. Yirmibeşoğlu, R. Kramer-Bottiglio, *Adv. Mater.* **2022**, 34, 2109617.
- [48] E. Brown, N. Rodenberg, J. Amend, A. Mozeika, E. Steltz, M. R. Zakin, H. Lipson, H. M. Jaeger, *Proc. Natl. Acad. Sci.* **2010**, 107, 18809.
- [49] Y.-J. Kim, S. Cheng, S. Kim, K. Iagnemma, *IEEE Trans. Robot.* **2013**, 29, 1031.
- [50] M. Manti, V. Cacucciolo, M. Cianchetti, *IEEE Robot. Autom. Mag.* **2016**, 23, 93.
- [51] B. Yang, R. Baines, D. Shah, S. Patiballa, E. Thomas, M. Venkadesan, R. Kramer-Bottiglio, *Sci. Adv.* **2021**, 7, eabh2073.
- [52] Y. S. Narang, A. Degirmenci, J. J. Vlassak, R. D. Howe, *IEEE Robot. Autom. Lett.* **2018**, 3, 688.
- [53] F. Caruso, G. Mantriota, L. Afferrante, G. Reina, *Mech. Mach. Theory* **2022**, 172, 104788.
- [54] V. Pini, J. J. Ruz, P. M. Kosaka, O. Malvar, M. Calleja, J. Tamayo, *Sci. Rep.* **2016**, 6, 29627.
- [55] S. Y. Kim, R. Baines, J. Booth, N. Vasios, K. Bertoldi, R. Kramer-Bottiglio, *Nat. Commun.* **2019**, 10, 1.